Critical influence of g-C$_3$N$_4$ self-assembly coating on the photocatalytic activity and stability of Ag/AgCl microspheres under visible light

Shifei Kang [a], Yao Fang [a], Yongkui Huang [a], Li-Feng Cui [b], Yunzhu Wang [b], Hengfei Qin [a], Yanmei Zhang [a], Xi Li [a,*], Yangang Wang [b,*]

[a] Department of Environmental Science and Engineering, Fudan University, Shanghai 200433, China
[b] Department of Environmental Science and Engineering, University of Shanghai for Science and Technology, Shanghai 200093, China

ARTICLE INFO

ABSTRACT

The g-C$_3$N$_4$ coated Ag/AgCl visible-light-driven photocatalysts were synthesized by a simple generic self-assembly approach at room temperature. The catalysts showed a uniform morphology with a controllable coating state on the scanning electron microscopy (SEM) and transmission electron microscopy (TEM) images. The wide structure and surface characterization showed that the presence of g-C$_3$N$_4$ notably affected the surface properties of Ag/AgCl photocatalysts. The photocatalytic activity was significantly dependent upon the coating ratio of g-C$_3$N$_4$ under visible light, while 1 wt% was the best coating ratio. Recycling experiments confirmed that the g-C$_3$N$_4$–Ag/AgCl catalysts had superior cycle performance and stability. These results suggested that the self-assembly g-C$_3$N$_4$ coating treatment had critical influence on the visible-light-driven photocatalytic activity and stability of Ag/AgCl plasmonic photocatalyst. The enhanced photocatalytic activity and stability could be ascribed to the formation of steady g-C$_3$N$_4$–Ag/AgCl heterojunction, which results in the efficient space separation of photo-induced charge carriers.

© 2015 Elsevier B.V. All rights reserved.

1. Introduction

Pollutants, especially textile dyestuffs and heavy-metal ions, have caused overwhelming environmental pollution worldwide. The effuents of these pollutants cannot be treated sufficiently or economically by traditional processes such as adsorption, ozonation and chlorination, which necessitates the development of novel cheap and efficient techniques [1,2]. In this instance, the techniques of photocatalysis, particularly visible-light-driven photocatalysis, are attractive, because they can transform environmental pollutants into non-hazardous compounds under visible light. Meanwhile, most photocatalysts are abundant, cheap, and environment-friendly [3].

Plasmonic photocatalysts which combine the advantages of noble metal nanoparticles (NPs) and semiconductor photocatalysts have recently attracted much attention, because they are expected to make a breakthrough in the field of photocatalysis. Ag/AgX(X = Cl, Br, I) is a series of important plasmonic photo-

catalysts that have been extensively studied. Huang et al. first synthesized Ag/AgCl particles with silver NPs formed on the surface, and the Ag/AgCl plasmonic photocatalyst was effective and stable under visible light [4]. Since then, many Ag/AgX plasmonic photocatalysts with high reactivity have been synthesized and intensively investigated [5–8]. In all these reports, Ag/AgX shows strong and broad absorption in the whole visible region owing to the localized surface plasmon resonance effects (LSPRs) of Ag NPs formed by photoreduction of pure silver halide (AgX) materials. The close contact between Ag NPs and AgX leads to an efficient separation between photogenerated electrons and holes, and thus to the drastic enhancement of photocatalytic activity during the visible-light-driven decomposition of environmental pollutants. The repeated treatments with Ag/AgX are used to bleach the environmental pollutants. The results indicate that this type of photocatalysts are basically stable under visible light irradiation, and thereby is potential in industrial water treatment [9–11]. Despite the great efforts, however, much work is left regarding the complex LSPR effects of plasmonic photocatalysts. Since the AgX materials are widely used as photosensitive agents in photographic films, the main challenge is how to improve the stability of Ag/AgX plasmonic photocatalysts.

* Corresponding authors. Tel.: +86 21 65642789; fax: +86 21 65642789.
E-mail addresses: xi_li@fudan.edu.cn (X. Li), ygwang8136@gmail.com (Y. Wang).

Great efforts have been devoted to the synthesis and characterization of Ag/AgX plasmonic photocatalysts with distinct structures, such as Ag/AgBr with high-index crystal facets exposure, [12] cubic Ag–AgCl hybrid NPs, [13] Ag–AgCl core–shell nanowires, [14] Ag/AgCl cubic cages, [15] and Ag/AgX with different sizes and morphologies [16–18]. However, to improve the photocatalytic efficiency and stability, a problem faced by these photocatalysts is photocorrosion [19]. In recent years, Ag/AgX plasmonic photocatalysts are widely combined with other semiconductors to improve their photocatalytic efficiency and stability. Many plasmonic semiconductor heterojunction photocatalysts have been developed, such as Ag/AgCl–ZnO, [19] Ag/Ag–WO$_3$·H$_2$O, [20] H$_2$WO$_4$·H$_2$O–Ag/AgCl, [21] Ag/AgCl–TiO$_2$, [22,23] and GO-Ag/AgX (X = Br, Cl) [24]. These composites all show enhanced photocatalytic efficiency and stability in decomposition of environmental pollutants and in antibiosis under visible light.

Currently, the novel visible-light-driven metal-free semiconductor g-C$_3$N$_4$ as a functional sensitizer has attracted wide attention from the photocatalysis field owing to its appealing electronic structure and medium band gap (2.7 eV) [25]. Similar to other conjugative π structure materials, g-C$_3$N$_4$ possesses rapid photo-induced charge separation ability and relatively slow charge recombination ability during electron transfer. Besides, the g-C$_3$N$_4$ photocatalyst is highly stable under thermal (up to 600 °C in air) or light irradiation in water as well as in acid or base solutions owing to its strong covalent bonds between carbon and nitride [26,27]. Coating g-C$_3$N$_4$ onto the surface of semiconductor photocatalysts could be an ideal approach to achieve enhanced and tunable photocatalytic activity [28].

In the present report, we describe a feasible and effective approach for self-assembly synthesis of g-C$_3$N$_4$ coated Ag/AgCl microspheres with strong photoreducing ability. The self-assembly coating process at room temperature was introduced in the surface treatment of plasmonic photocatalysts for the first time. The effects of molar ratio of g-C$_3$N$_4$ on formation morphology, structure and optical absorption ability of g-C$_3$N$_4$–Ag/AgCl photocatalysts were also investigated systematically. Ag/AgCl microspheres photocatalysts coated by 1 wt% g-C$_3$N$_4$ compared to uncoated Ag/AgCl plasmonic photocatalysts were more efficient and stable in photoreduction of organic dyes and Cr^{VI}. The photo-catalytic mechanism was tentatively analyzed.

2. Experimental

2.1. Materials and fabrication of g-C$_3$N$_4$ coated Ag/AgCl microspheres

All chemicals were purchased as analytical reagent (AR) grade from Shanghai Chemical Corp., and used without further purification.

2.1.1. Preparation of Ag/AgCl microspheres

Ag/AgCl microspheres were synthesized through simple oxidization of Ag NPs by Fe^{3+} at room temperature [29]. With Fe^{3+} as a mild controllable oxidant, all Fe-containing compounds were removed after the whole synthesis process, which maintained the pure phase of Ag/AgCl photocatalysts.

2.1.2. Preparation of g-C$_3$N$_4$ homogeneous suspension

Bulk g-C$_3$N$_4$ was prepared by simple calcination of melamine at 550 °C for 4 h in a covered alumina crucible, which prevented melamine from sublimation [30]. The as-prepared g-C$_3$N$_4$ was added into methanol and sonicated for 30 min, so that the bulk g-C$_3$N$_4$ was exfoliated into thin sheets and disintegrated into a homogeneous suspension.

2.1.3. Preparation of g-C$_3$N$_4$ coated Ag/AgCl microspheres

The g-C$_3$N$_4$ coated Ag/AgCl microspheres were synthesized with a simple self-assembly coating route (Fig. S1) at room temperature [31]. In a typical procedure, appropriate amounts of g-C$_3$N$_4$ and Ag/AgCl were added into methanol separately and sonicated for 30 min. Then the two suspensions were mixed and stirred at room temperature in the dark for 24 h. Afterwards, the mixture was evaporated in a rotary evaporator at 60 °C to remove the methanol, so that composite photocatalysts were prepared. The preparation procedure diagram is shown in Fig. S1. The g-C$_3$N$_4$ coated Ag/AgCl photocatalysts were labeled as ACN0.5, ACN1 and ACN2 depending on the weight ratio of g-C$_3$N$_4$ to Ag/AgCl; the pure Ag/AgCl photocatalyst was labeled as ACN0.

2.2. Characterization

The crystal structures of the as-prepared materials were identified using a Rigaku D/Max2rB–II X-ray diffractmeter (XRD, CuK1 radiation, λ = 1.5406 Å), operated at 40 kV and 100 mA (scanning step 4°/s). The particle size and morphologies of the materials were investigated using an FEI XL-30 scanning electron microscope (SEM), operated at an acceleration voltage of 25 kV. Transmission electron microscope (TEM) images were recorded using a JEOL JEM-2010 electron microscope with an acceleration voltage of 200 kV. The oxidation states of A, Ag, Cl, C and N on the material surfaces were determined by a PHI 5000 C ESCA X-ray photoelectron spectrometer (XPS) with Al Kα source at 14.0 kV and 25 mA. All the binding energies were referenced to the contaminant C 1s peak at 284.6 eV on the surface of adventitious carbon. Ultraviolent–visible (UV–vis) diffuse reflectance spectra (DRS) was achieved using a Shimadzu UV-2401 UV–vis spectrometer. Fourier transform infrared (FTIR) spectra were tested on a Nicolet Nexus 470 FTIR Spectrometer. The Raman spectra was recorded on a Horiba XploRA Raman microscope using a 532 nm argon ion laser.

2.3. Evaluation of photocatalytic activities

The photocatalytic activities were evaluated by studying the degradation of dye methyl orange (MO) and reduction of highly-toxic Cr^{VI} to low-toxicity Cr^{III} under visible light. The degradation of MO was performed by suspending a photocatalyst in an MO solution (50 mL, 10 mg/L). The reduction of Cr^{VI} was performed by suspending samples in a K$_2$CrO$_4$ solution (50 mL, 20 mg/L). The suspension was adjusted to pH 2 with dilute HClO$_4$, and also added with ethylene diamine tetraacetic acid (EDTA) as a sacrificial reagent. The optical system for detection of catalytic reaction included a 300 W Xe arc lamp (Phchem III, Beijing NBET Co., Ltd.) with a UV cutoff filter (providing visible light ≥420 nm). The solutions were stirred in the dark for 40 min until adsorption/desorption were balanced between the catalyst and contaminants. After a photocatalytic experiment was started by visible light irradiation, 1-mL aliquots were periodically withdrawn from the reaction vessel, diluted and centrifuged at 10,000 rpm for 5 min to separate the catalyst. The MO concentration was measured by a UV–vis spectrophotometer (Spectrumlab 752s, Xunda, Shanghai) at λ = 464 nm, while the Cr^{VI} concentration was measured using the diphenycarbazide (DPC) method at λ = 540 nm [32,33].

3. Results and discussion

3.1. Structure characterization

3.1.1. XRD

Fig. 1 showed the typical XRD patterns of pure g-C$_3$N$_4$, Ag/AgCl, and g-C$_3$N$_4$–Ag/AgCl photocatalysts. The major diffraction peaks marked with "●" at 2θ = 27.8, 32.2, 46.3, 54.8, 57.6, 67.4, 74.5 and
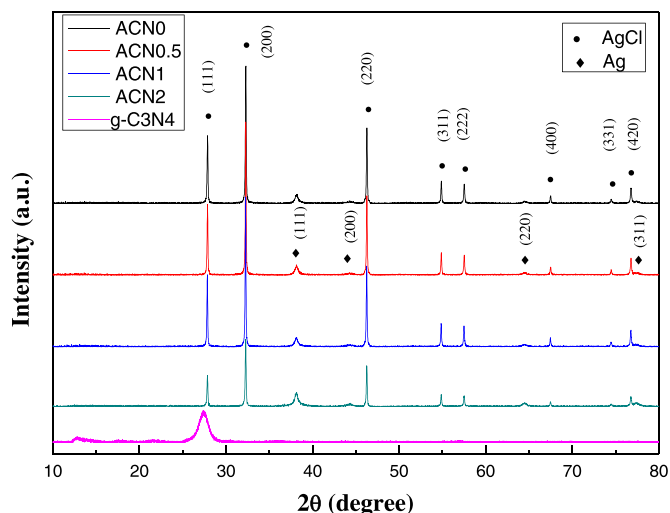
Fig. 1. XRD patterns of Ag/AgCl, g-C$_3$N$_4$ and g-C$_3$N$_4$–Ag/AgCl composites.

76.6° can be readily indexed to the reflections (1 1 1), (2 0 0), (2 2 0), (3 1 1), (2 2 2), (4 0 0), (3 3 1) and (4 2 0) of cubic-phase AgCl crystals (JCPDS card No. 31-1238), respectively. Besides, the weak peaks at 38.1, 44.3, 64.4, and 77.5° labeled as "♦" are assigned to the planes (1 1 1), (2 0 0), (2 2 0), and (3 1 1) of metallic cubic Ag^0 phase (JCPDS card No. 65-2871), respectively. According to Fig. 1, the as-obtained sample is an Ag/AgCl hybrid compound, and the content of metal Ag^0 is relatively low. Pure g-C$_3$N$_4$ shows two distinct diffraction peaks at 13.2 and 27.4°, corresponding to the peaks (1 0 0) and (0 0 2) of the graphitic phase, respectively [34]. The XRD patterns of the Ag/AgCl materials did not change notably after coating with g-C$_3$N$_4$ because of the low content (<2%) and the low XRD intensity of g-C$_3$N$_4$. Nevertheless, the presence of g-C$_3$N$_4$ was confirmed by energy dispersive spectrometry (EDS) and XPS. With the increasing g-C$_3$N$_4$ coating ratio, the g-C$_3$N$_4$–Ag/AgCl catalysts with different structures were obtained. The peaks of Ag^0 were obviously weakened, and the peaks of AgCl were enhanced after the addition of g-C$_3$N$_4$. The ratios of $I(1 1 1)/I(2 0 0)$ (Table 1) clearly show that the Ag^0 contents were quite different between the uncoated and the coated samples, indicating that the coating of g-C$_3$N$_4$ significantly restrained the decomposition of AgCl. ACN1 exhibits the lowest $I(1 1 1)/I(2 0 0)$ ratio, which means highest stability. No diffraction peak can be readily indexed to Fe-containing compounds in the as-prepared catalysts, which proved the absence of residual Fe^{3+} used in oxidization of Ag NPs. Thus, the Fe^{3+} oxidation route is simple and clear.

3.1.2. XPS

The states of element compositions in ACN0 and ACN1 were studied by XPS. The XPS spectra in Fig. 2a showed the typical strong peaks of Ag 3d, Cl 2p, C1s and N 1s. No other impurity peaks were detected, which proved the high purity of the resulting sample. The two strong peaks at around 367 and 373 eV on the high-resolution

(HR) spectrum (Fig. 2b) are assigned to Ag 3d$_{5/2}$ and Ag 3d$_{3/2}$, respectively. The spectrum of Ag 3d$_{5/2}$ s is further split into two peaks at 367.6 and 368.4 eV, while the spectrum of Ag 3d$_{3/2}$ is further split into two peaks at 373.6 and 374.3 eV. The peaks at 368.4 and 374.3 eV are characteristic of Ag^0, which significantly proved the presence of Ag NPs in the g-C$_3$N$_4$–Ag/AgCl composites. In addition, the core levels of Cl 2p show the dominant peaks around 199 eV (Fig. 2c), which is consistent with the Cl$^-$ state. The ratio of Ag/Cl$^-$ in ACN1 calculated from XPS spectra is 0.83 (lower than 1, the original ratio of Ag^0/Cl$^-$), and thus, the redundant Cl$^-$ accumulated on the surface of g-C$_3$N$_4$–Ag/AgCl composites, which benefited the photodegradation. The spectrum of C 1s can be shown into one peak around 284.61 eV (Fig. 2d), which is ascribed to carbon and defect-containing sp^2-bonded carbon. Fig. 2e shows the HR XPS spectra of N 1s. The main N 1s peak with binding energy of 398.73 eV can be attributed to sp^2-hybridized nitrogen (C=N—C) [35]. All these results confirm the coexistence of Ag/AgCl and g-C$_3$N$_4$ in ACN1. Besides, no Fe-containing compound I left on the surface of the catalysts, which further confirmed the absence of residual Fe^{3+} in the composites. These results are in compliance with the XRD results.

3.1.3. FTIR spectra

Fig. 3 shows the FT-IR spectra of pure g-C$_3$N$_4$, ACN0, ACN0.5, ACN1, and ACN2. The spectrum of pure g-C$_3$N$_4$ shows the strong bands within 1200–1650 cm^{-1}, with peaks at 1238, 1320, 1406, 1459, 1547, 1572 and 1639 cm^{-1}, which correspond to the typical stretching vibration modes of C—N and C—N heterocycles [36,37]. Additionally, pristine carbon nitride exhibits the typical band around 808 cm^{-1} corresponding to the breathing mode of the heptazine arrangement (synphase and antiphase vibrations of N—N of tetrazine ring) [38]. The FT-IR spectra of ACN0.5, ACN1, and ACN2 all show the main characteristic peaks of g-C$_3$N$_4$, which is consistent with XPS analysis. Besides, a wide band between 3000 and 3400 cm^{-1} was also observed, which corresponds to the N—H stretching vibration of residual NH$_2$ attached to the sp2-hybridized carbon [39]. The peaks of NH$_2$ band are quite weak in ACN0 and ACN0.5, but are enhanced in ACN1 and ACN2. These bands in the composite materials corresponded to the O—H stretching of the superficial free OH group. Furthermore, ACN1 exhibits the richest superficial bands, especially within 1300–1700 cm^{-1}, which means a high surface reaction performance.

3.1.4. Raman spectra

The Raman spectra further confirm the presence of g-C$_3$N$_4$ in the g-C$_3$N$_4$–Ag/AgCl composites revealed by FTIR. Fig. 4 shows the Raman spectra of ACN0, pure g-C$_3$N$_4$, and the g-C$_3$N$_4$–Ag/AgCl composites. The spectrum of pure g-C$_3$N$_4$ shows several strong distinctive peaks of g-C$_3$N$_4$ at 458, 693 and 1217 cm^{-1}[36]. With the increase of g-C$_3$N$_4$ coating ratio, the weak main Raman bands of g-C$_3$N$_4$ were found in the spectra of g-C$_3$N$_4$–Ag/AgCl composites. ACN0 shows much stronger Raman peaks at 610, 1198, 1363, 1507, 1542 and 1649 cm^{-1} (Fig. 4), which are attributed to the Surface Enhanced Raman Scattering (SERS) of AgCl [40]. However, the

Table 1
Physical properties of pure g-C$_3$N$_4$, ACN0, ACN0.5, ACN1 and ACN2.

Sample	R	IAg^0(1 1 1)/I AgCl (2 0 0)	S$_{BET}$ (cm^2 g^{-1})	PV (cm^{-3} g^{-1})	APS
g-C$_3$N$_4$	–	–	9.69	0.33	42.84
ACN0	0	20.4%	0.81	0.07	30.95
ACN0.5	0.005	6.4%	1.00	0.08	28.75
ACN1	0.01	6.0%	0.93	0.06	29.53
ACN2	0.02	6.3%	0.98	0.06	25.78

R: weight ratio of g-C$_3$N$_4$ to Ag/AgCl.
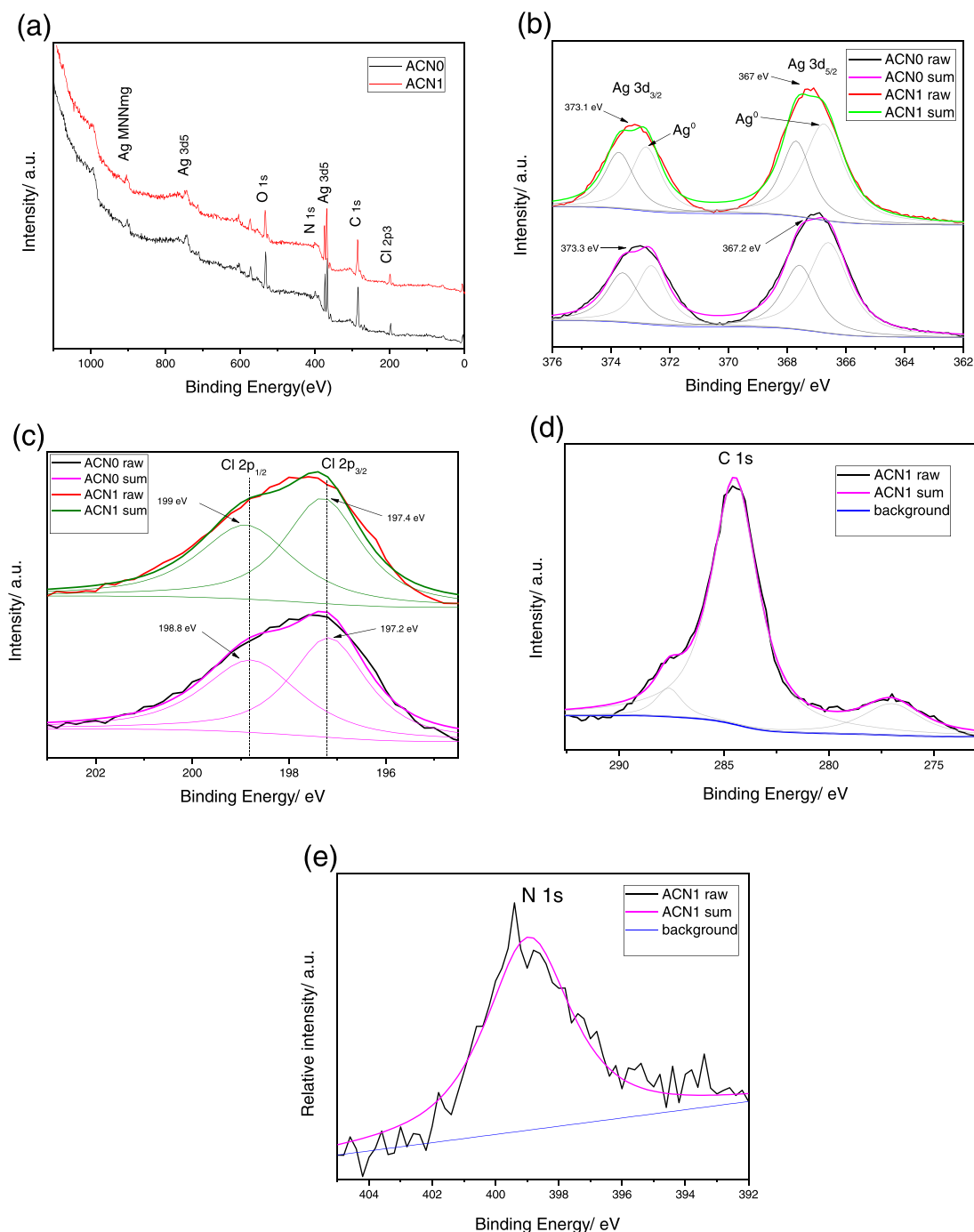PV: pore volume.
APS: average pore size.

Fig. 2. XPS spectra of ACN0 and ACN1: (a) survey scan spectrum, (b) high-resolution spectra of Ag 3d, and (c) Cl 2p. Typical spectra of (d) C 1s and (e) N 1s from ACN1.

characteristic peaks of AgCl were weakened significantly in ACN1 and ACN2, indicating that the surface-coated g-C$_3$N$_4$ can control the excessive SERS activity and improve the stability of Ag/AgCl catalysts.

3.2. Morphologic characterization

3.2.1. SEM

Fig. 5 shows the typical SEM images of ACN0 (Fig. 5a–d) and the pure bulk g-C$_3$N$_4$ (Fig. 5e–f). Clearly, ACN0 is in well-dispersed sphere-like structure with an average diameter of 1–2 μm, which is in good agreement with a former report using the same ferric iron oxidation method. And the microspheres constructed from

AgCl NPs are in size 100–200 nm, and self-supported pores are formed by the aggregation of AgCl NPs. It should be noticed that numerous tiny nanoparticles with size about 10 nm appear just like islands on the surface of AgCl microspheres (Fig. 5d), which might be Ag NPs formed by natural photoreduction of pure AgCl. Fig. 5f also shows that the bulk g-C$_3$N$_4$ was constructed from substantial g-C$_3$N$_4$ nanosheets. The SEM images of ACN0.5 (Fig. 5g–h), ACN1 (Fig. 5i–j) and ACN2 (Fig. 5k–l) show similar sphere-like structures as ACN0, but their surfaces are increasingly rougher with the increase of g-C$_3$N$_4$ coating content. The large-scale SEM images of g-C$_3$N$_4$–Ag/AgCl composites and more detailed SEM images of over-coated ACN2 are shown in Figs. S2 and 3, respectively. The crystallite sizes are almost the same, indicating that the coating of
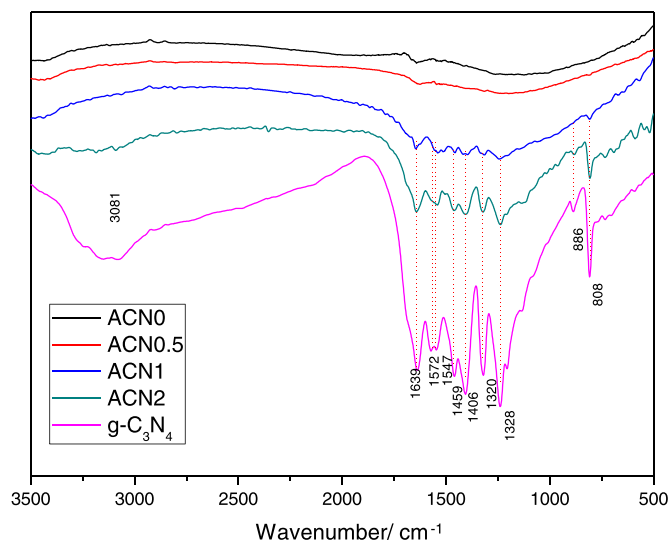
Fig. 3. FT-IR spectra of pure g-C_3N_4, ACN0, ACN0.5, ACN1, and ACN2.

Fig. 4. Raman spectra of pure g-C_3N_4, ACN0, ACN0.5, ACN1, and ACN2.

g-C_3N_4 did not change the fundamental structure of Ag/AgCl plasmonic photocatalysts. The island-like Ag NPs can also be observed at the surface of 1% wt g-C_3N_4 coated Ag/AgCl microspheres, which ensured good visible light absorption characteristics of ACN1 samples. The enlarged SEM image of ACN1 (Fig. 5j) shows that the g-C_3N_4 nanosheets are dispersed over the surface of the microspheres, which formed a thin coating layer. This g-C_3N_4 layer may help to improve the stability of Ag/AgCl photocatalysts.

3.2.2. TEM

The structures of ACN1 and ACN4 were further examined with TEM. An HR-TEM image of ACN1 (Fig. 6a–b) clearly reveals the interface between g-C_3N_4 and Ag/AgCl microspheres. The thin g-C_3N_4 layer with a thickness of 5–10 nm was observed in ACN1, this coating layer was unclosed in some places. These results demonstrate that ACN1 is a composite rather than a physical mixture of g-C_3N_4 and Ag/AgCl, while the transfer channels for radicals and dyestuff molecules are unblocked. Such a structural feature is beneficial
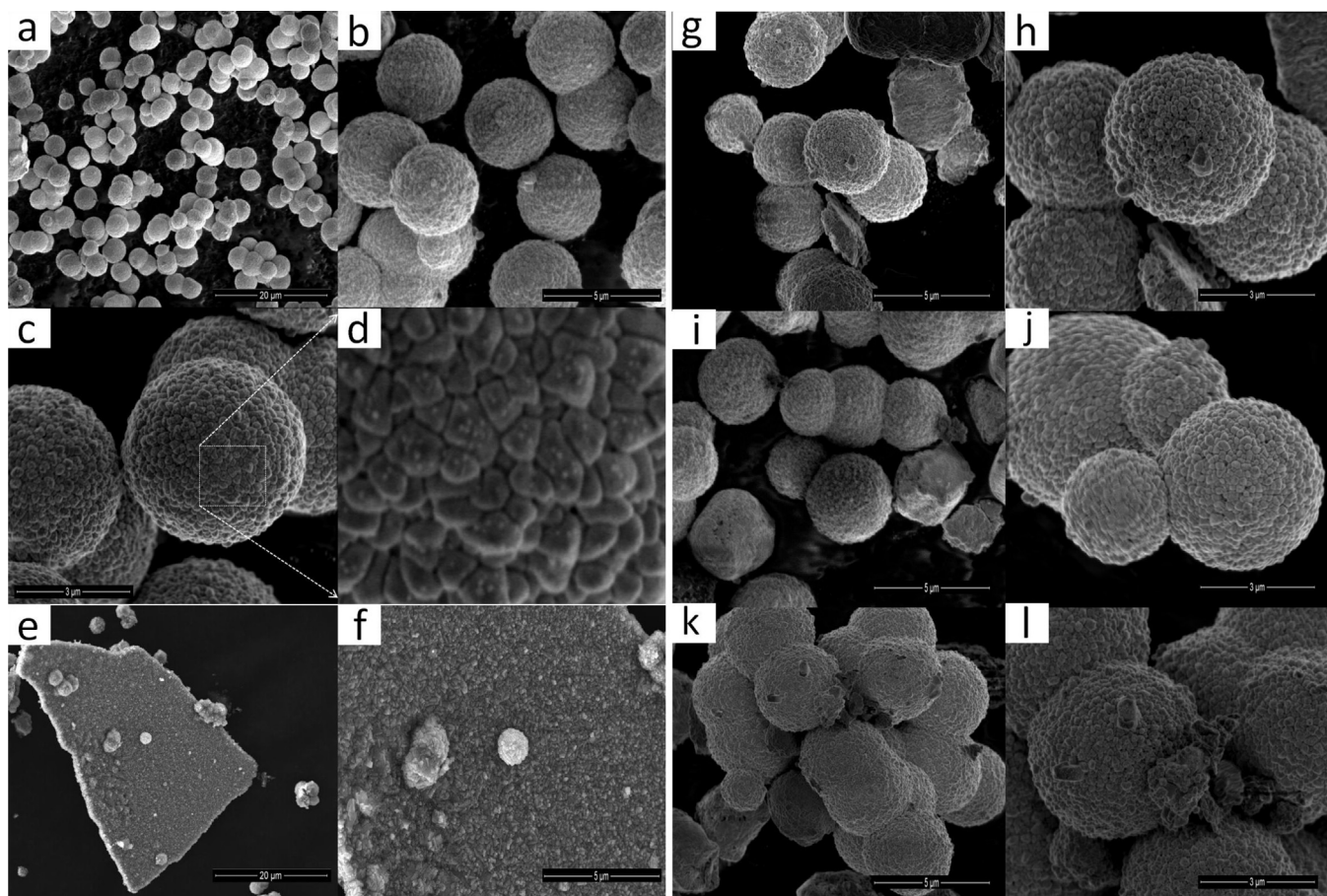

Fig. 5. SEM images of ACN0(a–d), pure g-C_3N_4(e–f), ACN0.5(g–h), ACN1(i–j), and ACN2(k–l).
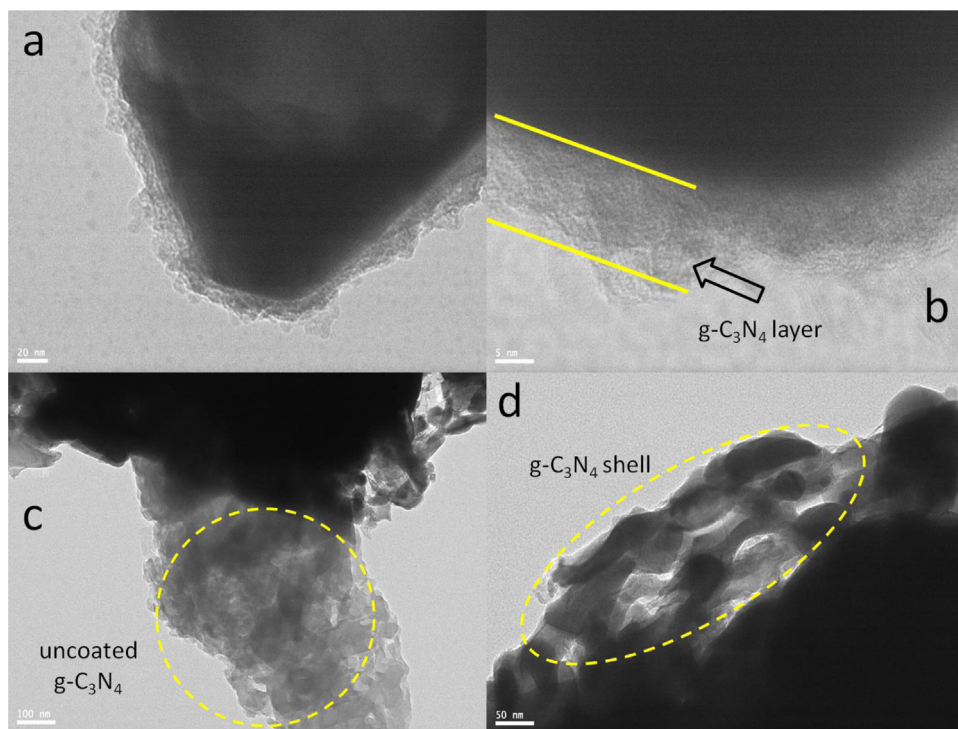
Fig. 6. TEM images of ACN1(a–b) and ACN2(c–d) samples.

for efficient separation of charge carriers, which will be discussed later. To investigate the effects of g-C$_3$N$_4$ content on the growth of g-C$_3$N$_4$–Ag/AgCl hybrid composites, ACN2 (Fig. 6c–d) was synthesized from a two-fold amount of g-C$_3$N$_4$ under the same condition. The coating of 2 wt% g-C$_3$N$_4$ in ACN2 resulted in the formation of abundant massive uncoated g-C$_3$N$_4$ bulk (Fig. 6c), as well as a much more compact g-C$_3$N$_4$ shell (Fig. 6d). Furthermore, the element distributions of ACN1 and ACN2 were further studied using EDS mapping. The results (Fig. S4) proved the existence of C and N in the g-C$_3$N$_4$-coated sample, which is consistent with XPS and FITR results.

3.3. Nitrogen adsorption analysis

Nitrogen adsorption and desorption isotherms were plotted to characterize the specific surface areas (SSAs) of the g-C$_3$N$_4$–Ag/AgCl composites, and the results are showed in Fig. 7 and S5. The isotherms of ACN0, ACN0.5, ACN1 and ACN2 are similarly type IV with hysteresis loops according to the International Union of Pure and Applied Chemistry (IUPAC) classification, indicating the presence of mesopores. The low-pressure hysteresis loop ($0.4 < P/P_0 < 0.9$) is related to the intra-aggregated pores of g-C$_3$N$_4$–Ag/AgCl composites, and the high-pressure hysteresis loop ($0.9 < P/P_0 < 1$) is probably associated with the larger pores formed between secondary particles. The Brunauer–Emmett–Teller SSAs (S_{BET}), pore volumes, and average pore sizes of all samples are summarized in Table 1. The S_{BET} is $0.81\,m^2\,g^{-1}$ in ACN0, and then increases to $1.00\,m^2\,g^{-1}$ in ACN0.5. However, the S_{BET} decreases with a further increase of C$_3$N$_4$ content. The variations in S_{BET} may relate to the changes in pore size. The insets of size distribution in Figs. 7 and S5b shows the S_{BET} of the g-C$_3$N$_4$–Ag/AgCl composites. The pristine Ag/AgCl contains mesopores in size of 25–50 nm. The presence of a small amount of g-C$_3$N$_4$ can introduce a number of small mesopores (2–25 nm) and thus decrease the average pore size from 30.95 nm (in ACN0) to less than 25 nm (28.75 nm in ACN0.5 and 29.53 nm in ACN1). Since the pore volumes of all the samples

do not change appreciably, the S_{BET} of ACN0.5 increases accordingly. However, further increase of g-C$_3$N$_4$ content may subject the Ag/AgCl photocatalysts to adhesion and aggregation, which in turn reduces the amount of mesopores and increases the average pore size. Consequently, S_{BET} decreases.

3.4. UV–vis DRS spectra

Fig. 8a shows the UV–vis DRS spectra of the samples. Strong absorption occurs throughout the UV region, which is characteristic of Ag. Interestingly, pure g-C$_3$N$_4$ almost did not respond optically in the visible light region of 400–750 nm, while Ag/AgCl and the g-C$_3$N$_4$–Ag/AgCl photocatalysts exhibited broad absorption, owing to the surface plasmon resonance (SPR) of Ag NPs

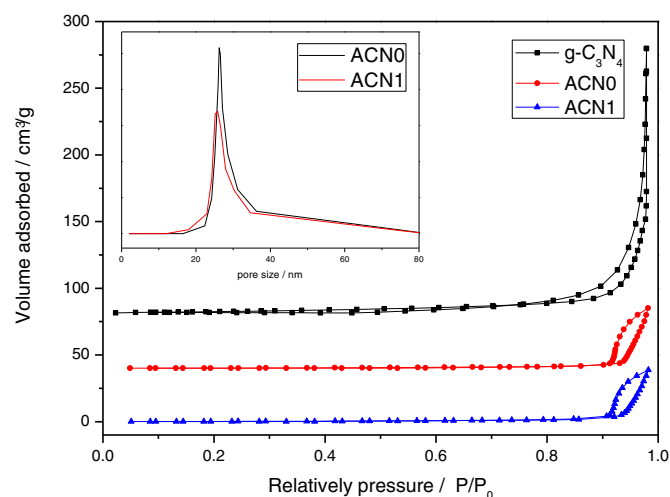**Fig. 7.** Nitrogen adsorption–desorption isotherms for pure g-C$_3$N$_4$, ACN0 and ACN1. Inset shows the corresponding pore size distributions of ACN0 and ACN1 calculated by the BJH method.
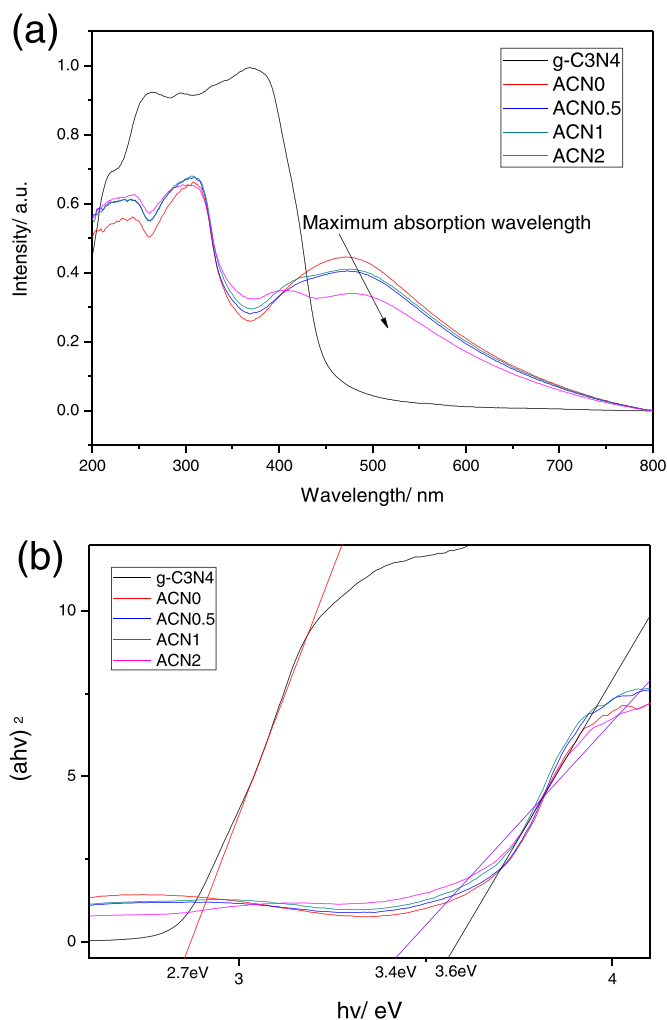
Fig. 8. (a) UV–vis absorption spectra (in the diffuse reflectance spectra mode) of pure g-C$_3$N$_4$, ACN0, ACN0.5, ACN1, and ACN2. (b) Plots of (ahν)^2 vs. energy (hν) of the samples.

Fig. 9. Photodecomposition of (a) MO dye and (b) Cr^{VI} in solutions (a.10 mgL^{-1}, b.20 mgL^{-1}) over pure g-C$_3$N$_4$, ACN0, ACN0.5, ACN1, and ACN2 under visible-light irradiation (λ > 420 nm). C is the concentration of MO dye at time t, and C$_0$ that in the MO solution immediately after it is kept in the dark to reach the equilibrium adsorption state.

originating from the photodegradation of AgCl. In accordance with the previous assumption, we found that the visible light absorption intensity was weakened after coating. When the g-C$_3$N$_4$ coating ratio increased, the maximum absorption wavelength red-shifted, meaning that the band gap of g-C$_3$N$_4$-coated samples was reduced. This can also be proved by plots of ahν vs. energy (hν) for the band gap energy of g-C$_3$N$_4$–Ag/AgCl samples in Fig. 8b. Besides, the indirect semiconductor band gap of g-C$_3$N$_4$–Ag/AgCl samples is calculated to be 3.4–3.6 eV, which is larger than the energy of visible light, indicating that the visible light absorption ability is mainly supported by Ag NPs rather than by the AgCl semiconductor. The LSPR effect contributed prominently to the enhanced photocatalytic activity.

4. Discussion of photocatalytic activity

4.1. Photocatalytic Activity and Photostability.

The photocatalytic activities of the samples were evaluated by the separate degradation of MO and Cr^{VI} in solutions under visible-light irradiation. Prior to visible-light irradiation, the MO and Cr^{VI} solutions with a catalyst were kept in the dark for 40 min to reach adsorption equilibrium. Fig. 9a shows the MO degradation rates in the aqueous solution in the presence of a photocatalyst under visible-light irradiation, where C_0 is the MO concentration
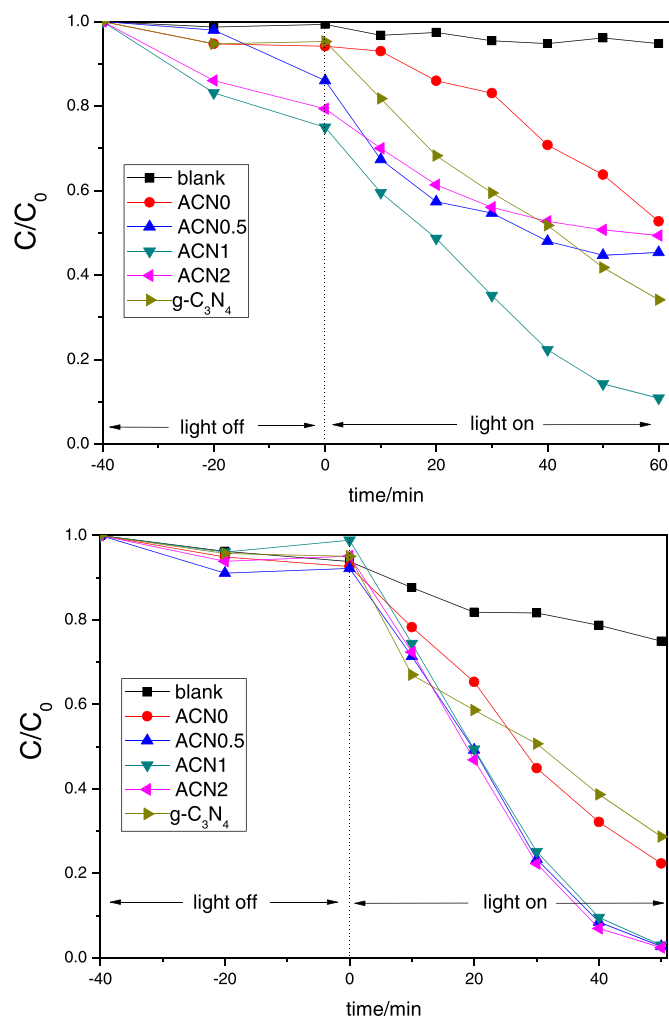
under equilibrium, and C is that after visible-light irradiation. The results show that the degradation of MO hardly occurred in the dark or under visible-light irradiation without g-C$_3$N$_4$–Ag/AgCl. The visible-light degradation results of g-C$_3$N$_4$–Ag/AgCl photocatalysts indicated that g-C$_3$N$_4$–Ag/AgCl composites were highly photocatalytic for MO reduction. The concentration of MO decreased with the increasing irradiation time, as nearly half of MO was photo-reduced only after 20 min of irradiation with the presence of ACN1, and almost all MO was reduced after 60 min. Moreover, the MO degradation efficiencies were 47.3%, 53.7%, 89.2%, 50.7% and 65.9% with the presence of ACN0, ACN0.5, ACN1, ACN2 and g-C$_3$N$_4$, respectively, indicating that MO was degraded more efficiently by g-C$_3$N$_4$–Ag/AgCl than by the pure Ag/AgCl or g-C$_3$N$_4$. Provided that the reaction follows a pseudo-first order procedure, the MO decomposition rate by ACN1 was estimated to be 2.97 μg min^{-1}, which was higher compared with ACN0, ACN0.5 and ACN2 (1.58, 1.79 and 1.69 μg min^{-1}, respectively). Fig. 9b displays the similar photodegradation efficiencies of Cr^{VI}–Cr^{III} under visible-light irradiation. The photodegradation activity of Ag/AgCl was improved significantly after coating with g-C$_3$N$_4$. However, compared with photodegradation of MO, the reduction effect of surface coating amount on Cr^{VI} was inconspicuous, which will be discussed later. In addition, the results of photodegradation of 4-chlorophenol (4-CP)
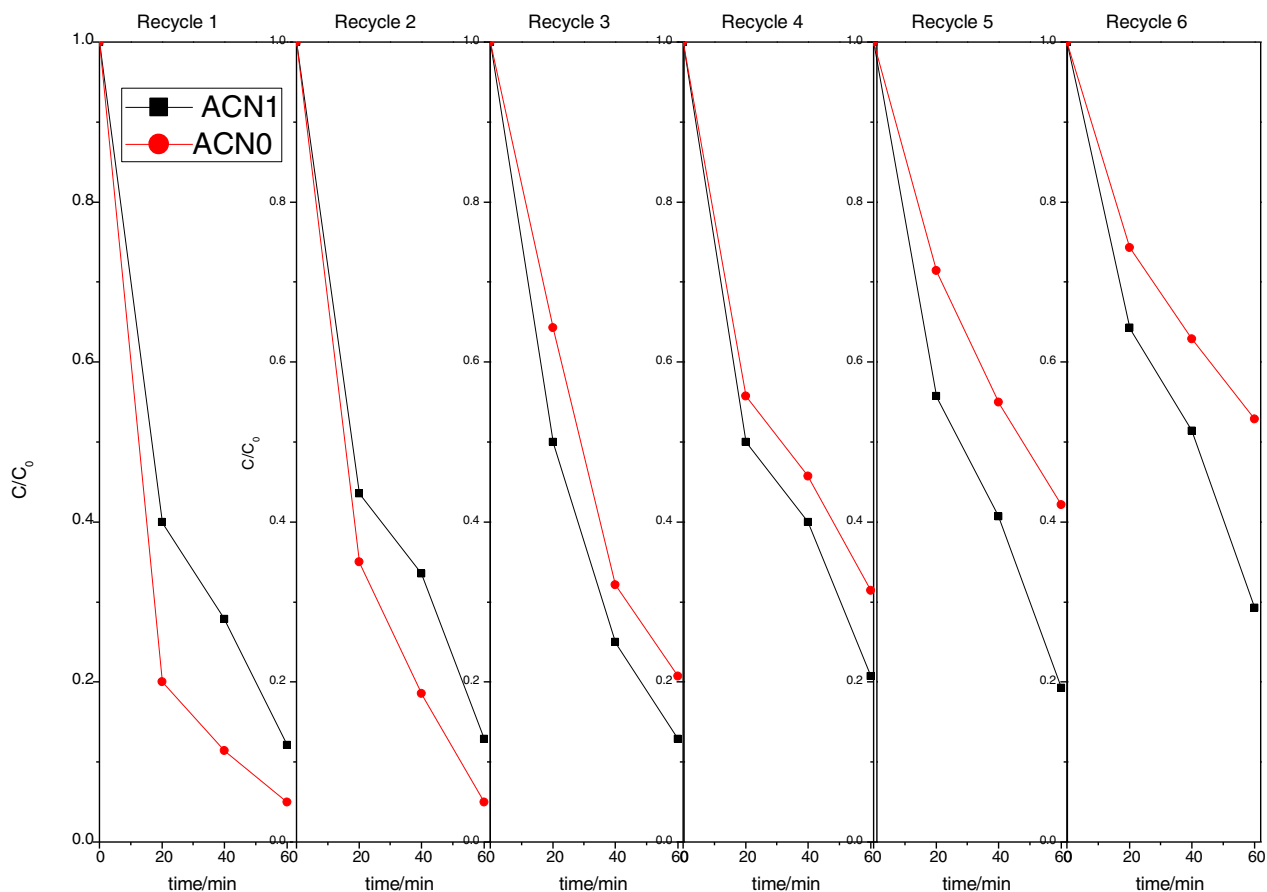
Fig. 10. Time course of photodecomposition for MO dye. The reaction photocatalysts were washed by centrifugation at the end of each cycle to remove the organic residues inside.

under visible light can further prove the universal photocatalytic activity of g-C_3N_4 coated Ag/AgCl plasmonic photocatalyst (Fig. S6).

The stability of an environmental photocatalyst is also very important in terms of applications. The stability of the g-C_3N_4–Ag/AgCl composites was further evaluated by reusing the catalysts after the visible-light degradation of MO (Fig. 10). The amount of ACN0 was doubled to make a similar initial velocity. After six cycles of MO photocatalytic degradation, the activity of g-C_3N_4–Ag/AgCl catalyst was not reduced significantly, confirming that the g-C_3N_4–Ag/AgCl composites are effective and stable during the photocatalysis. Fig. 11 shows the comparison on XRD patterns between fresh ACN1 and ACN1 used for photodecomposition against MO dye after 6 cycles. The intensities of diffraction peaks of AgCl and metallic Ag both decreased after five recycles, indicating that the pholocatalyst might partly run off with the prolonging of washing time. However, the typical patterns of diffraction peaks of AgCl and metallic Ag in ACN1 did not change significantly, indicating that the g-C_3N_4 coating layer efficiently improved the stability of Ag/AgCl. Therefore, the photocatalytic performance of the g-C_3N_4–Ag/AgCl composites was not weakened. This result is similar to a previous report [41].

4.2. Mechanisms of Photocatalytic Activity Enhancement and Photocorrosion Suppression.

Generally, photocatalytic activity is mainly governed by light-absorption ability, surface properties (e.g., adsorption property and SSA), and photogenerated charge- separation efficiency. As reports by peers, in Ag/AgCl photocatalyst system, because of the surface plasmon resonance effect of silver NPs, the yields

of the photogenerated electrons and holes can be significant increased [42]. Subsequently, femtosecond transient absorption spectroscopy proved that the electron transfer process from Ag NPs to the AgCl surface is ultrafast ($\leq$150 fs), which facilitates the charge separation efficiency, thus contributing to high photocatalytic activity of Ag/AgCl photocatalyst towards organic contaminants degradation [15,43]. What's more, the g-C_3N_4 coating on the surface of Ag/AgCl photocatalysts can form an effective
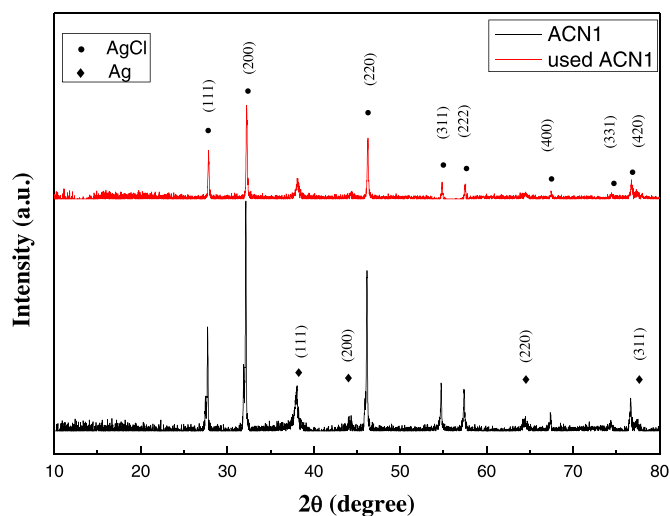

Fig. 11. Comparison on XRD patterns of fresh ACN1 and ACN1 used for photodecomposition against MO dye after 6 cycles.
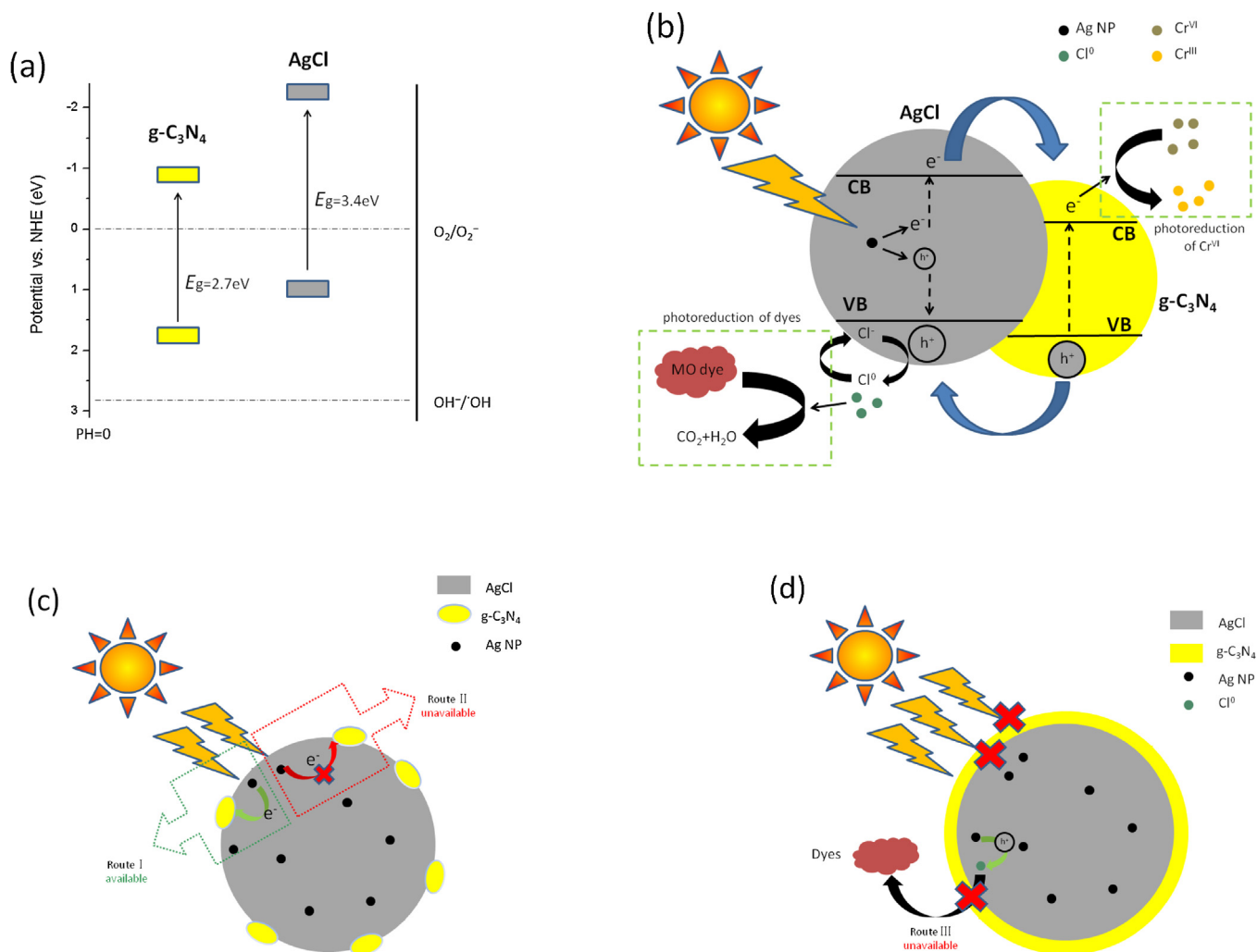
Fig. 12. Schematic illustration of (a) band positions of g-C$_3$N$_4$ and Ag/AgCl together with OH$^-$/˙OH and O$_2$/O$_2^-$ redox potentials, (b) the energy-level configuration and the photogenerated charge-transfer between g-C$_3$N$_4$ and Ag/AgCl, (c) the photocatalytic process on a Ag/AgCl microsphere with a thin and unclosed g-C$_3$N$_4$ layer, and (d) a Ag/AgCl microsphere with a dense and closed g-C$_3$N$_4$ shell.

heterojunction electric fieldon the interface between g-C$_3$N$_4$ and Ag/AgCl, resulting in significantly strengthened separation of the photogenerated electrons and holes, thus can further increase the visible light absorption intensity while suppress the photocorrosion [44]. As discussed above, however, the coating of g-C$_3$N$_4$ did not substantially affect the light-absorption property or S_{BET} (0.81 m^2 g^{-1} for ACN0 and 0.93 m^2 g^{-1} for ACN1), indicating that these two factors are not correlated with the photocatalytic activity of g-C$_3$N$_4$–Ag/AgCl composites. Therefore, the enhancement of photocatalytic activity after coating may be mainly attributed to the synergic effect between g-C$_3$N$_4$ and Ag/AgCl, which can greatly accelerate the separation of photogenerated carriers.

Fig. 12a illustrates the schematic representation of the energy-level configuration and the photogenerated charge-transfer in g-C$_3$N$_4$–Ag/AgCl composites. According to previous studies, the NHE conduction band (CB) and valence band (VB) of AgCl are at about −2.1 and 1.3 eV, respectively, while those of bulk g-C$_3$N$_4$ are at −0.85 and 1.85 eV, respectively. Under the excitation of visible light, the SPR effect produced by the collective electron oscillation on the surface of Ag NPs can enhance the local inner electromagnetic field (Fig. 12b). Owing to the local electromagnetic field and the high visible-light absorption capability of Ag NPs, the excited electrons can be transferred quickly and farthermost from Ag NPs to the CB of AgCl, which helps to stabilize AgCl. The abundant pho-

togenerated electrons on the CB of AgCl can be readily injected into the CB of g-C$_3$N$_4$, whereas the photogenerated holes on VB of g-C$_3$N$_4$ can be directly transferred to the VB of AgCl. Therefore, after coating of a proper amount of g-C$_3$N$_4$ (R$_{CN}$ < 1 wt%) onto Ag/AgCl, the excited energetic electrons on Ag/AgCl can be injected into g-C$_3$N$_4$ and then participate in the photocatalytic reaction on the uncovered areas of AgCl together with the photogenerated holes on AgCl. Meanwhile, the photogenerated electrons on AgCl can rapidly migrate to the coated g-C$_3$N$_4$, which basically alleviates the photocorrosion of AgCl. In this case, an effective charge separation is achieved, which then results in photocatalytic activity enhancement and photocorrosion inhibition (RouteIin Fig. 12c). It should be noticed that with too low coating amount (RouteIIin Fig. 12c), the photogenerated electrons on AgCl cannot efficiently migrate to the g-C$_3$N$_4$ coating layer, and thus the heterojunction effect is reduced, which explains the superior photocatalytic activity of ACN1 compared with ACN0.5.

However, with the increased g-C$_3$N$_4$ content, a dense and unopen shell around AgCl is gradually formed (Fig. 12d). In this case, the closed shell prevents AgCl from contacting the reaction solution. Thus, the number of holes in the VB of AgCl significantly is reduced and cannot sufficiently react with the adsorbed Cl$^-$ to form Cl^0-related radicals. Moreover, the limited Cl^0 cannot carry out oxidation against MO. Generally, Cl^0 related radicals are regarded as

the main active free radical in AgCl plasmonic photocatalysts, and play the key role during photocatalysis by transforming environmental pollutants into non-hazardous compounds. Furthermore, the holes will accumulate on the interface of AgCl, which may lead to a serious recombination of electron-hole pairs. Consequently, the synergic effect between g-C$_3$N$_4$ and AgCl diminishes drastically and the photocatalytic activity will be weakened rapidly with further increase of g-C$_3$N$_4$ content. Importantly, the g-C$_3$N$_4$ content in g-C$_3$N$_4$–Ag/AgCl composites should be prudently controlled.

The mechanism of Cr^{VI} photoreduction is approximately similar as MO degradation, the only difference is that the reduction reaction mainly occurs on the surface of g-C$_3$N$_4$, because the CB of g-C$_3$N$_4$ is located below that of AgCl. Thus, the electrons on the CB of AgCl are transferred into the VB of g-C$_3$N$_4$ to produce reactive superoxide radical ion ($^\bullet$O$_2^-$) or other active radicals, these electrons and functioning radicals will facilitate the reduction of Cr^{VI}. Since the electrons transfer property of g-C$_3$N$_4$ layer is poor, the active reaction surface was limited mainly on the direct contact interface of g-C$_3$N$_4$ and AgCl [8]. Therefore, it is not surprising that the reduction effect of g-C$_3$N$_4$ coating content on Cr^{VI} is inconspicuous.

5. Conclusions

The g-C$_3$N$_4$ coated Ag/AgCl photocatalysts were prepared via a simple one-step impregnation method at room temperature. Characterization tests confirmed the introduced g-C$_3$N$_4$ layer with a thickness of 5–10 nm covered the surface of the Ag/AgCl microsphere, resulting in increased visible light absorption intensity due to the SPR effect of Ag NPs. The g-C$_3$N$_4$ coating treatment affected the photocatalytic activity of Ag/AgCl notably compared with the uncoated Ag/AgCl photocatalyst and pure g-C$_3$N$_4$, and the optimal g-C$_3$N$_4$ content was 1 wt%. More importantly, the photocatalytic activity of the uncoated Ag/AgCl microsphere was severely weakened after 6 cycles, while the 1 wt% g-C$_3$N$_4$ coated Ag/AgCl material was highly photostable. The photocatalytic activity enhancement and photocorrosion suppression of g-C$_3$N$_4$ coating on Ag/AgCl microsphere under visible light were induced, which was attributed to the formation of the g-C$_3$N$_4$–Ag/AgCl photocatalytic heterojunction system, thus enhenced the efficient space separation of electron–hole pairs. However, Ag/AgCl plasmonic photocatalyst covered by superfluous g-C$_3$N$_4$ would suffer from a rapid irradiation reduction due to the shielding effect of g-C$_3$N$_4$ layer, which become a recombination centre of the lingered photogenerated electrons and holes. The g-C$_3$N$_4$–Ag/AgCl heterojunction structure was proved as a very promising candidate for practical application in high-performance photoreduction of textile dyestuffs and heavy-metal ions. Furthermore, the present study provides unprecedented insights for fabricating other functional plasmonic photocatalysts.

Acknowledgements

Appendix A. Supplementary data

Supplementary data associated with this article can be found, in the online version, at http://dx.doi.org/10.1016/j.apcatb.2015.01.002.

References

[1] T. Robinson, G. McMullan, R. Marchant, P. Nigam, Remediation of dyes in textile effluent: a critical review on current treatment technologies with a proposed alternative, Bioresour. Technol. 77 (2001) 247–255.

[2] C.C. Chen, W.H. Ma, J.C. Zhao, Semiconductor-mediated photodegradation of pollutants under visible-light irradiation, Chem. Soc. Rev. 39 (2010) 4206–4219.

[3] H.L. Wang, L.S. Zhang, Z.G. Chen, J.Q. Hu, S.J. Li, Z.H. Wang, J.S. Liu, X.C. Wang, Semiconductor heterojunction photocatalysts: design, construction, and photocatalytic performances, Chem. Soc. Rev. 43 (2014) 5234–5244.

[4] P. Wang, B.B. Huang, X.Y. Qin, X.Y. Zhang, Y. Dai, J.Y. Wei, M.H. Whangbo, Ag@AgCl: a highly efficient and stable photocatalyst active under visible light, Angew. Chem. Int. Ed. 47 (2008) 7931–7933.

[5] P. Wang, B.B. Huang, X.Y. Zhang, X.Y. Qin, H. Jin, Y. Dai, Z.Y. Wang, J.Y. Wei, J. Zhan, S.Y. Wang, J.P. Wang, M.H. Whangbo, Highly efficient visible-light plasmonic photocatalyst Ag@AgBr, Chem-Eur. J. 15 (2009) 1821–1824.

[6] P. Wang, B.B. Huang, X.Y. Qin, X.Y. Zhang, Y. Dai, M.H. Whangbo, Ag/AgBr/WO$_3$ center dot H$_2$O: visible-light photocatalyst for bacteria destruction, Inorg. Chem. 48 (2009) 10697–10702.

[7] H.F. Cheng, B.B. Huang, P. Wang, Z.Y. Wang, Z.Z. Lou, J.P. Wang, X.Y. Qin, X.Y. Zhang, Y. Dai, In situ ion exchange synthesis of the novel Ag/AgBr/BiOBr hybrid with highly efficient decontamination of pollutants, Chem. Commun. 47 (2011) 7054–7056.

[8] P. Wang, B.B. Huang, X.Y. Zhang, X.Y. Qin, Y. Dai, Z.Y. Wang, Z.Z. Lou, Highly efficient visible light plasmonic photocatalysts Ag@Ag(Cl,Br) and Ag@AgCl–AgI, Chemcatchem 3 (2011) 360–364.

[9] Z.F. Bian, T. Tachikawa, P. Zhang, M. Fujitsuka, T. Majima, Au/TiO$_2$ superstructure-based plasmonic photocatalysts exhibiting efficient charge separation and unprecedented activity, J. Am. Chem. Soc. 136 (2014) 458–465.

[10] J.T. Li, S.K. Cushing, J. Bright, F.K. Meng, T.R. Senty, P. Zheng, A.D. Bristow, N.Q. Wu, Ag@Cu$_2$O core–shell nanoparticles as visible-light plasmonic photocatalysts, Acs Catal. 3 (2013) 47–51.

[11] Z.K. Zheng, B.B. Huang, X.Y. Qin, X.Y. Zhang, Y. Dai, M.H. Whangbo, Facile in situ synthesis of visible-light plasmonic photocatalysts M@TiO$_2$ (M = Au, Pt, Ag) and evaluation of their photocatalytic oxidation of benzene to phenol, J. Mater. Chem. 21 (2011) 9079–9087.

[12] H. Wang, J.T. Yang, X.L. Li, H.Z. Zhang, J.H. Li, L. Guo, Facet-dependent photocatalytic properties of AgBr nanocrystals, Small 8 (2012) 2802–2806.

[13] R.F. Dong, B.Z. Tian, C.Y. Zeng, T.Y. Li, T.T. Wang, J.L. Zhang, Ecofriendly synthesis and photocatalytic activity of uniform cubic Ag@AgCl plasmonic photocatalyst, J. Phys. Chem. C 117 (2013) 213–220.

[14] Y.P. Bi, J.H. Ye, In situ oxidation synthesis of Ag/AgCl core–shell nanowires and their photocatalytic properties, Chem. Commun. (2009) 6551–6553.

[15] Y.X. Tang, Z.L. Jiang, G.C. Xing, A.R. Li, P.D. Kanhere, Y.Y. Zhang, T.C. Sum, S.Z. Li, X.D. Chen, Z.L. Dong, Z. Chen, Efficient Ag@AgCl cubic cage photocatalysts profit from ultrafast plasmon-induced electron transfer processes, Adv. Funct. Mater. 23 (2013) 2932–2940.

[16] C.H. An, S.N. Peng, Y.G. Sun, Facile synthesis of sunlight-driven AgCl:Ag plasmonic nanophotocatalyst, Adv. Mater. 22 (2010) 2570–2574.

[17] L.Q. Ye, J.Y. Liu, C.Q. Gong, L.H. Tian, T.Y. Peng, L. Zan, Two different roles of metallic ag on AG/AGX/BIOX (x = cl, br) visible light photocatalysts: surface plasmon resonance and Z-scheme bridge, Acs Catal. 2 (2012) 1677–1683.

[18] H.X. Shi, J.Y. Chen, G.Y. Li, X. Nie, H.J. Zhao, P.K. Wong, T.C. An, Synthesis and characterization of novel plasmonic Ag/AgX-CNTs (X = Cl, Br I) Nanocomposite photocatalysts and synergetic degradation of organic pollutant under visible light, Acs Appl. Mater. Inter. 5 (2013) 6959–6967.

[19] W.B. Li, F.X. Hua, J.G. Yue, J.W. Li, Ag@AgCl plasmon-induced sensitized ZnO particle for high-efficiency photocatalytic property under visible light, Appl. Surf. Sci. 285 (2013) 490–497.

[20] D.L. Chen, T. Li, Q.Q. Chen, J.B. Gao, B.B. Fan, J. Li, X.J. Li, R. Zhang, J. Sun, L. Gao, Hierarchically plasmonic photocatalysts of Ag/AgCl nanocrystals coupled with single-crystalline WO$_3$ nanoplates, Nanoscale 4 (2012) 5431–5439.

[21] X.F. Wang, S.F. Li, Y.Q. Ma, H.G. Yu, J.G. Yu, H$_2$WO$_4$ center dot H$_2$O/Ag/AgCl composite nanoplates: a plasmonic Z-scheme visible-light photocatalyst, J. Phys. Chem. C 115 (2011) 14648–14655.

[22] Y. Hou, X.Y. Li, Q.D. Zhao, X. Quan, G.H. Chen, TiO$_2$ nanotube/Ag-AgBr three-component nanojunction for efficient photoconversion, J. Mater. Chem. 21 (2011) 18067–18076.

[23] J.G. Yu, G.P. Dai, B.B. Huang, Fabrication and characterization of visible-light-driven plasmonic photocatalyst Ag/AgCl/TiO$_2$ TiO$_2$ nanotube arrays, J. Phys. Chem. C 113 (2009) 16394–16401.

[24] M.S. Zhu, P.L. Chen, M.H. Liu, Graphene oxide enwrapped Ag/AgX (X = Br, Cl) Nanocomposite as a highly efficient visible-light plasmonic photocatalyst, Acs Nano 5 (2011) 4529–4536.

[25] X.C. Wang, K. Maeda, A. Thomas, K. Takanabe, G. Xin, J.M. Carlsson, K. Domen, M. Antonietti, A metal-free polymeric photocatalyst for hydrogen production from water under visible light, Nat. Mater. 8 (2009) 76–80.

[26] Y. Wang, X.C. Wang, M. Antonietti, Polymeric graphitic carbon nitride as a heterogeneous organocatalyst: from photochemistry to multipurpose catalysis to sustainable chemistry, Angew. Chem. Int. Ed. 51 (2012) 68–89.

[27] A.J. Du, S. Sanvito, Z. Li, D.W. Wang, Y. Jiao, T. Liao, Q. Sun, Y.H. Ng, Z.H. Zhu, R. Amal, S.C. Smith, Hybrid graphene and graphitic carbon nitride nanocomposite: gap opening, electron-hole puddle, interfacial charge

transfer, and enhanced visible light response, J. Am. Chem. Soc. 134 (2012) 4393–4397.

[28] L. Zhang, D.W. Jing, X.L. She, H.W. Liu, D.J. Yang, Y. Lu, J. Li, Z.F. Zheng, L.J. Guo, Heterojunctions in g-C$_3$N$_4$/TiO$_2$(B) nanofibres with exposed (0 0 1) plane and enhanced visible-light photoactivity, J. Mater. Chem. A 2 (2014) 2071–2078.

[29] B.W. Ma, J.F. Guo, W.L. Dai, K.N. Fan, Highly stable and efficient Ag/AgCl core–shell sphere: controllable synthesis, characterization, and photocatalytic application, Appl. Catal. B-Environ. 130 (2013) 257–263.

[30] S.C. Yan, Z.S. Li, Z.G. Zou, Photodegradation performance of g-C$_3$N$_4$ fabricated by directly heating melamine, Langmuir 25 (2009) 10397–10401.

[31] C.S. Pan, J. Xu, Y.J. Wang, D. Li, Y.F. Zhu, Dramatic activity of C$_3$N$_4$/BiPO$_4$ photocatalyst with core/shell structure formed by self-assembly, Adv. Funct. Mater. 22 (2012) 1518–1524.

[32] Y.C. Dai, G.R. Qian, Y.L. Cao, Y. Chi, Y.F. Xu, J.Z. Zhou, Q. Liu, Z.P. Xu, S.Z. Qiao, Effective removal and fixation of Cr(VI) from aqueous solution with Friedel's salt, J. Hazard. Mater. 170 (2009) 1086–1092.

[33] M. Wang, Y.B. Chen, F. Wu, Y.F. Su, L. Chen, D.L. Wang, Characterization of yttrium substituted LiNi^0 33Mn^0 33Co^0 33O$_2$ cathode material for lithium secondary cells, Electrochim. Acta 55 (2010) 8815–8820.

[34] G.H. Dong, L.Z. Zhang, Porous structure dependent photoreactivity of graphitic carbon nitride under visible light, J. Mater. Chem. 22 (2012) 1160–1166.

[35] L. Ge, C.C. Han, J. Liu, Y.F. Li, Enhanced visible light photocatalytic activity of novel polymeric g-C$_3$N$_4$ loaded with Ag nanoparticles, Appl. Catal. a-Gen. 409 (2011) 215–222.

[36] Q.J. Xiang, J.G. Yu, M. Jaroniec, Preparation and enhanced visible-light photocatalytic H-2-Production activity of graphene/C$_3$N$_4$ composites, J. Phys. Chem. C 115 (2011) 7355–7363.

[37] Y.J. Wang, R. Shi, J. Lin, Y.F. Zhu, Enhancement of photocurrent and photocatalytic activity of ZnO hybridized with graphite-like C$_3$N$_4$, Energy Environ. Sci. 4 (2011) 2922–2929.

[38] X.S. Zhou, Z.H. Luo, P.F. Tao, B. Jin, Z.J. Wu, Y.S. Huang, Facile preparation and enhanced photocatalytic H-2-production activity of Cu(OH)(2) nanospheres modified porous g-C$_3$N$_4$, Mater. Chem. Phys. 143 (2014) 1462–1468.

[39] H.J. Yan, H.X. Yang, TiO$_2$-g-C$_3$N$_4$ composite materials for photocatalytic H-2 evolution under visible light irradiation, J. Alloy. Compd. 509 (2011) L26–L29.

[40] C.B. Dong, Z.J. Yan, J. Kokx, D.B. Chrisey, C.Z. Dinu, Antibacterial and surface-enhanced Raman scattering (SERS) activities of AgCl cubes synthesized by pulsed laser ablation in liquid, Appl. Surf. Sci. 258 (2012) 9218–9222.

[41] R. Guo, G.K. Zhang, J. Liu, Preparation of Ag/AgCl/BiMg$_2$VO$_6$ composite and its visible-light photocatalytic activity, Mater. Res. Bull. 48 (2013) 1857–1863.

[42] M.S. Zhu, P.L. Chen, W.H. Ma, B. Lei, M.H. Liu, Template-free synthesis of cube-like Ag/AgCl nanostructures via a direct-precipitation protocol: highly efficient sunlight-driven plasmonic photocatalysts, Acs Appl. Mater. Inter. 4 (2012) 6386–6392.

[43] C.H. An, J.Z. Wang, C. Qin, W. Jiang, S.T. Wang, Y. Li, Q.H. Zhang, Synthesis of Ag@AgBr/AgCl heterostructured nanocashews with enhanced photocatalytic performance via anion exchange, J. Mater. Chem. 22 (2012) 13153–13158.

[44] Y.Y. Bu, Z.Y. Chen, C. Feng, W.B. Li, Study of the promotion mechanism of the photocatalytic performance and stability of the Ag@AgCl/g-C$_3$N$_4$ composite under visible light, Rsc Adv. 4 (2014) 38124–38132.